Growth Hormone & IGF Research 77 (2024) 101607

Contents lists available at ScienceDirect

Growth Hormone & IGF Research

journal homepage: www.elsevier.com/locate/ghir

Using site-directed mutagenesis to further the understanding of insulin receptor-insulin like growth factor-1 receptor heterodimer structure

Samuel Turvey [a], Stephen P. Muench [b], Tarik Issad [c], Colin W.G. Fishwick [d], Mark T. Kearney [a], Katie J. Simmons [b,*]

[a] Leeds Institute for Cardiovascular and Metabolic Medicine, University of Leeds, Leeds, UK
[b] School of Biomedical Sciences, Faculty of Biological Sciences & Astbury Centre, University of Leeds, UK
[c] Université Paris Cité, CNRS, INSERM, Institut Cochin, F-75014 Paris, France
[d] Department of Chemistry University of Leeds, Leeds, UK

ARTICLE INFO

Keywords:
Insulin receptor
IGF-1 receptor
Mutagenesis
Alphafold

ABSTRACT

Type 2 diabetes is characterised by the disruption of insulin and insulin-like growth factor (IGF) signalling. The key hubs of these signalling cascades - the Insulin receptor (IR) and Insulin-like growth factor 1 receptor (IGF1R) – are known to form functional IR-IGF1R hybrid receptors which are insulin resistant. However, the mechanisms underpinning IR-IGF1R hybrid formation are not fully understood, hindering the ability to modulate this for future therapies targeting this receptor. To pinpoint suitable sites for intervention, computational hotspot prediction was utilised to identify promising epitopes for targeting with point mutagenesis. Specific IGF1R point mutations F450A, R391A and D555A show reduced affinity of the hybrid receptor in a BRET based donor-saturation assay, confirming hybrid formation could be modulated at this interface. These data provide the basis for rational design of more effective hybrid receptor modulators, supporting the prospect of identifying a small molecule that specifically interacts with this target.

1. Introduction

Over the past five decades changes in human lifestyle have contributed to an explosion of obesity [1] and its frequent sequelae insulin resistant type 2 diabetes mellitus. [2] A poorly understood hallmark of obesity and type 2 diabetes mellitus is disruption of insulin signalling, [3,4] leading to dysregulation of cellular growth and nutrient handling. [5] The insulin receptor (IR) acts as a conduit for insulin-encoded information, which is transferred *via* a complex intracellular signalling network including the critical signalling nodes phosphatidylinositol 3-kinase (PI3-K) and the serine/threonine kinase Akt, to regulate cell metabolism. [6] During evolution the IR and insulin-like growth factor-1 receptor (IGF1R) diverged from a single receptor in invertebrates, [7,8] into a more complex system in mammals. [9] Stimulation of IR or IGF1R initiates phosphorylation of IR substrate (IRS) proteins at multiple tyrosine residues, [6] phosphorylated IRS1 binds PI3-K initiating the conversion of the plasma lipid phosphatidylinositol 3,4,-bisphosphate to phosphatidylinositol 3,4,5-trisphosphate (PIP3) which activates the multifunctional serine−threonine kinase Akt. [10] In endothelial cells Akt activates the endothelial isoform of nitric oxide synthase (eNOS) by phosphorylation of serine 1177. [11,12] In humans and other mammals despite high structural homology and activation of similar downstream pathways the biological processes regulated by insulin and IGF-1 are strikingly different. [13] Consistent with this in endothelial cells Kearney et al. demonstrated that deletion of IR reduced, [14,15] whereas deletion of IGF1R increased basal serine 1177 phosphorylated eNOS and insulin-mediated phosphorylation of serine 1177 on eNOS. [16] They also showed that increasing IR in endothelial cells enhances insulin-mediated serine phosphorylation of Akt but blunts insulin-mediated serine 1177 phosphorylation of eNOS, [17] whereas increased IGF1R reduces basal serine 1177 phosphorylated eNOS and insulin-mediated serine 1177 phosphorylation of eNOS. [18]

The Insulin receptor (IR) and Insulin-like growth factor receptor (IGF1R) are closely related multi-domain receptor tyrosine kinases (RTKs) that share *ca.* 70% sequence homology. The IR is activated through binding to insulin, whilst IGF1R is activated through binding to the hormones Insulin-like growth factor (IGF) 1 and IGF2. [19] Upon binding to their respective ligands, IR primarily regulates metabolic

* Corresponding author.
E-mail address: K.J.Simmons@leeds.ac.uk (K.J. Simmons).

https://doi.org/10.1016/j.ghir.2024.101607
Received 4 April 2024; Received in revised form 26 June 2024; Accepted 17 July 2024
Available online 18 July 2024

signalling through the PI3K/AKT pathway, whilst IGF1R elicits mitogenic effects through the Ras/ERK pathway. However, there is substantial crossover in the signalling of the receptors through the shared signalling nodes of the Insulin receptor substrate 1, IRS2 and Shc. Similarly, the IR and IGF1R can both bind to insulin, IGF1 and IGF2, albeit with varying affinities. [20–22] Due to the array of signalling pathways regulated by the IR and IGF1R, aberrant signalling through these receptors is associated with several diseases. Specifically, dysfunctional insulin signalling is the primary driver of type 2 diabetes mellitus, whilst altered IGF1 signalling manifests in several forms of cancer due to its role modulating cell proliferation. [23]

IR and IGF1R are unique amongst RTK's in that they exist on the cell surface membrane as preformed dimers, contrasting with other RTK's that only dimerise upon ligand binding. This means that the receptors share a unique mode of action amongst RTK's; hormone binding elicits a large-scale conformational change to activate the receptor. The structural basis of activation of the insulin family receptors is still not fully understood, although recent findings have significantly contributed towards providing a plausible activation mechanism of the receptors. [24] Ligands binding to the extracellular portion (ectodomain) of the receptors affect trans-autophosphorylation of the intracellular kinase domains, which in turn promotes binding and phosphorylation of adaptor proteins to affect subsequent downstream signalling.

Due to their high homology, the IR and IGF1R can heterodimerise to form functional hybrid receptors in tissues in which they are co-expressed, consisting of an IR monomer and IGF1R monomer. Hybrid receptors bind IGF1 with *ca.* fifty times higher affinity than insulin and *ca.* ten times higher affinity than IGF2. [20–22] The physiological role, signalling properties and mechanisms regulating the formation of IR-IGF1R hybrid receptors are currently poorly understood. However, it is believed that hybrid receptors confer insulin resistance by sequestering IR protein and reducing the available insulin binding sites on the cell surface. [25,26] Similarly, increased numbers of hybrid receptors may increase the number of receptors binding IGF1 and IGF2, and therefore contribute to the signalling of these receptors in certain cancers. [27] In skeletal muscle, fat and the heart, hybrid formation has been shown to exceed that of IGF1R and IR dimers. [28] While the role of hybrids in human physiology is undefined there is a clear association with increased hybrids and situations of metabolic stress including: type 2 diabetes mellitus, [29,30] obesity, [31] hyperinsulinemia, [31] insulin resistance [32] and hyperglycaemia.[33]Whilst there have been significant recent advances in the structural information available for the IR and IGF1R, limited structural information exists for hybrid receptors [34], especially without IGF1 bound. Here we seek to further our understanding of hybrid formation using homology modelling and site-directed mutagenesis.

2. Materials and methods

2.1. Transfection of HEK293 cells

HEK293 (ATCC, CRL3022) cells cultured in high-glucose DMEM supplemented with 10% (*v*/v) FBS, 2 mM L-glutamine, and 1% penicillin/streptomycin were seeded into a 6 well plate at 2.5×10^6 cells per well and incubated (24 h) to achieve approximately 70% confluency by transfection. Transfections were performed with Lipofectamine 2000 (Invitrogen) and cDNAs at a ratio of 5:1 (*v/w*). The transfected cells were then incubated for at least 12 h before harvesting or replating for further assays. Plasmids encoding the constructs IR-Rluc, IGF1R-Rluc, IR-YPET and IGF1R-YPET were gifts from Dr. Tariq Issad (INSERM institute, Paris).

2.2. BRET assay

HEK293 cells were seeded into 6-well plates at a density of 2.5×10^5 cells per well and transfected as above. Cells were co-transfected with IR-Rluc cDNA (0.3 μg) and either IGF1R-YPET cDNA (0.3 μg) or empty pUC19 cloning vector cDNA (0.3 μg) to bring the total DNA to 0.6 μg per well. Transfected cells were incubated for 24 h. After 24 h the transfected cells would typically be imaged using an Incucyte® Zoom (Sartorius) live cell imager to check the expression of YPET labelled protein and ensure transfection efficiency. Subsequently the cells were washed with DPBS (1 mL) (Sigma Aldrich) and the transfected cells pooled to reduce the effects of variation in well to well transfection efficiency. The cells were seeded into 96 well plate at a density of 1.5×10^4 cells per well and incubated for 24 h before changing into serum free DMEM and incubating for a further 24 h. Prior to plate reading, IGF1 (Antibodies.com) dissolved in deionised water was added to each well at a final concentration of 100 nM and incubated for 15 mins. Measurements were performed on a Envision® 2105 Multimode Plate Reader (Perkin Elmer). A solution of coelenterazine-h in ethanol (250 mM, 1 mL) was added to each well to give a final concentration of 5 mM in each well. Light-emission acquisition at 485 nm and 535 nm was started immediately. BRET signal was expressed in milliBRET unit (mBU). The BRET unit has been defined previously as the ratio 535 nm/485 nm obtained when the two partners are present, corrected by the ratio 535 nm/485 nm obtained under the same experimental conditions, when only the partner fused to *Renilla luciferase* is present in the assay. This can be represented as:

$$BRET = (E535 \div E485) - Cf$$

Where E_{535} corresponds to the luminescence at 535 nm, E_{485} corresponds to the luminescence at 485 nm, and *Cf* corresponds to the ratio E_{535}/E_{485} for the Rluc tagged construct transfected alone.

2.3. IGF1 treatment

Cell culture and transfections were performed as above. After 24 h post transfection, cells were changed into serum free DMEM (Gibco), containing no FBS supplement, and incubated (24 h). IGF1 (antibodies.com) dissolved in deionised water was added to each well at a final concentration of 100 nM and incubated (37 °C, 15 mins). Subsequently, the BRET ratio was measured as described above.

2.4. Western blotting sample preparation

HEK293 cells were transfected with 0.3 μg of the relevant cDNA per well. After 24 h, cells were washed with ice-cold DPBS (1 mL) (Sigma Aldrich) and each well lysed by addition of lysis buffer (80 μL) (Invitrogen) on ice. The lysates were pre-cleared by centrifugation (14,000 *g* for 10 min at 4 °C).

2.5. Western blotting

The protein concentration of cell lysates was determined using the Pierce BCA Protein Assay Kit (Thermo Scientific). 50 μg of protein was mixed with NuPAGE™ LDS sample loading buffer (4×) (Invitrogen), NuPAGE™ sample reducing buffer (10×) (Invitrogen) and water to give the appropriate sample volume, before heating to 95 °C for 5 mins to ensure protein denaturation. Samples were loaded onto NuPAGE™ 4 to 12%, Bis-Tris gels (Invitrogen) alongside molecular weight markers samples and separated by SDS-PAGE electrophoresis for 90 mins at 110 V. Samples were then transferred to nitrocellulose membranes (Bio-Rad) using the TransBlot® Turbo Transfer System (Bio-Rad). The membrane was dried and incubated in 2% BSA TBST for 1 h to block non-specific binding. Membranes were treated overnight with primary antibodies at the relevant concentrations. Subsequently, the membranes were washed 3 × 10 mins in TBST before treatment with horseradish-peroxidase conjugated secondary antibodies of the relevant species (1:5000) in 5% BSA TBST for 1 h. The membranes were then washed in 3 × 10 mins in TBST before visualisation. The antibodies used in this study are detailed in the supplementary information (Supplemental

Table 4).

2.6. Protein visualisation

The immunoreactive proteins were visualised using the Western Chemiluminescent HRP substrate reagents (Immobilon) before imaging on the G:Box (Syngene) system. Blots were then stripped by application of stripping buffer for 15 mins before 3 × 10 mins of washes with TBST. Membranes were stored dry at 4 °C. Images were analysed using the Image J software [35], with each band normalised to the signal of β-actin from the same sample for analysis.

2.7. Fluorescence microscopy

HEK293 cells were maintained and transfected as above. Cells were transfected with IR-Rluc and empty pUC19 vector, or IR-Rluc and IGF1R-YPET mutants and incubated (24 h). The media was then replaced with OptiMEM (1 mL) (Gibco), and cells imaged on an EVOS cell imaging system (ThermoFisher) utilising the GFP filter.

2.8. Mutagenesis

Site directed mutagenesis was performed with Platinum™ SuperFi™ DNA polymerase (Invitrogen) using the manufacturers protocol. Primers were designed with NEBasechanger (https://nebasechanger.neb.com/) and primer sequences are supplied in the supplementary information (Supplemental Table 3). Mutations were confirmed by DNA sequencing (Supplemental fig. 5).

2.9. Donor saturation assay

HEK293 cells were seeded into a 12 well plate with 2×10^5 cells per well and incubated for 24 h. The cells were co-transfected using 110 ng of IR-Rluc per well and increasing ratios (0–20 x) of IGF1R-YPET (wild-type (WT) or mutant), with empty pUC19 to maintain total DNA at 2130 ng per well. Transfections were performed at approximately 60% confluency. Plasmid DNA was diluted in OptiMEM (200 μL) (Gibco) and PEI (11.5 μL of a 1 mg mL^{-1}, 5:1 *w*/w PEI: DNA) (Polysciences) added to the DNA solution. The solution was immediately vortexed (5 s) and incubated (RT, 15 mins). The transfection mixture (200 μL) was added dropwise to each well and the plate rocked to ensure even distribution over the well. The cells were incubated with the transfection reagents for 4 h, after which the media was exchanged for fresh media and the cells incubated for a further 44 h. Cells were then seeded at 5×10^5 per well into white 96-well plate and incubated for 24 h. Simultaneously, the cells were seeded into a black 96 well plate. Cells were washed with DPBS (200 uL per well) (Sigma Aldrich) and resuspended in DPBS (50 μL). BRET measurements were recorded as above. Fluorescence measurements were recorded at 535 nm after excitation at 513 nm on cells in black plates.

2.10. Radioligand binding assay

HEK293 cells were seeded into 6-well plates at 2.5×10^6 cells per well. After 24 h, the cells were transfected with WT IR-Rluc or WT IGF1R-YPET as above. Several transfections were performed using either 0.15, 0.30 or 0.6 μg cDNA per well. 24 h later, cells were plated into a 96-well plate with 50,000 cells per well and incubated for a further 24 h. Subsequently, the cells were washed with DPBS (100 μL per well) (Sigma Aldrich) and then maintained in DPBS (50 uL). For IR-Rluc transfected cells, coelenterazine-h was added to a final concentration of 5 μM and the luminescence recorded at 485 nm. For IGF1R-YPET transfected cells, the fluorescence at 535 nm was recorded for each well after excitation at 513 nm.

For radioligand binding, ^{125}I-insulin or ^{125}I-IGF1 (PerkinElmer) were diluted to the working concentration with unlabelled insulin or IGF1 respectively. This was then further diluted in DPBS to give six separate ligand concentrations spanning 0.5–10 times the Kd value for the relevant receptor-ligand complex. An aliquot of each radioligand was then removed and unlabelled insulin or IGF1 added at a final concentration of 500 nM (*ca.* 100 x Kd) to allow the measurement of non-specific radioligand binding. A further aliquot of radioligand was retained to determine the specific activity of each radioligand concentration. The radioligand was then added to the cells in duplicate wells for each concentration value and the cells incubated (3 h, 37 °C). Post-incubation, the cells were washed with ice-cold DPBS (100 μL) and lysed by addition of cell lysis buffer (50 μL) (Invitrogen). Cell lysates were removed into counting vials, and each well washed further lysis buffer (50 μL). Vials were counted on an AMG Automated Gamma Counter (Hidex). The K_d and B_{max} values were determined using GraphPad Prism using non-linear regression model with single site fitting.

2.11. TACOS model generation

Sequences for residues 332–619 of the human IR-B and 331–608 of the human IGF1R downloaded from the UniProt Databse [36–38]. These were submitted to the TACOS online structure prediction server (https://zhanglab.ccmb.med.umich.edu/TACOS/) with default settings.

2.12. AlphaFold model generation

Sequences for residues 332–619 of the human IR-B and 331–608 of the human IGF1R downloaded from the UniProt Databse [37–39]. These were submitted to the ColabFold [40] using Alphafold2 multimer [41] using 20 recycles with tolerance = 0.05. pLDDT values and the PAE plot were downloaded from the results file UCSF ChimeraX [42] used to visualise the resulting model.

2.13. Homology model quality assessment

Models were submitted to the SWISS-MODEL (https://swissmodel.expasy.org/) structure assessment server [43–45]. QMEANDisCO values were downloaded and visualised in UCSF ChimeraX [42].

2.14. Hotspot prediction

Hotspot prediction using the resulting IR-IGF1R hybrid models was performed using KFC2 server (https://mitchell-web.ornl.gov/KFC_Server/index.php) [46]. Visualisation of the homology model and hotspot analysis was performed using UCSF ChimeraX [42].

2.15. Statistics

Data were analysed using GraphPad Prism software (version 9)[195]. *P* values >0.05 were deemed statistically significant. Results are expressed as mean ± SEM unless otherwise stated.

Comparisons between two groups were performed using an unpaired Student's *t*-test. Comparisons between the mean values of multiple groups were performed using one-way analysis of variance (ANOVA), followed by Tukey's multiple comparisons test. Non-linear regression curves were calculated using a single-site fitting model, accounting for non-specific binding if appropriate.

3. Results and discussion

3.1. Homology modelling of IR IGF1R hybrid receptors

As several related structures of the unliganded IR and IGF1R had been determined, [47,48] homology modelling provided a viable route for building a structural model of the apo-IR-IGF1R hybrid receptor. The published IR and IGF1R apo-receptor structures were examined to

determine the major interfaces forming between the two receptor monomers. In both receptors, three separate interfaces form: between the L1: FnIII-2′ domains, the L2: FnIII-1′ domains and between the αCT: L1'. With these interfaces present in both the IR and IGF1R structures, it was reasoned that the same interfaces were likely to form in the IR-IGF1R hybrid receptor. Of these, the L2: FnIII-1′ interface was chosen as it encompassed the largest contact area, and therefore may be expected to contribute significantly towards hybrid dimerisation. This interface does not lie at the ligand binding sites which have been established for the IR and IGF1R [49–51]. The TACOS [52] (Template-based Assembly of COmplex Structures) server was initially chosen to produce the model as it is designed to model the structures of protein-protein complexes.

Sequence alignments were performed using MUSTER [53] on residues 332–619 of the IR-B (UniProt ID: P06213–1) and 331–608 of the IGF1R (UniProt ID: P08069). TACOS identified the IR crystal structure (PDB:4ZXB) as the best template for the global protein complex, with 68% identity and 86% coverage. The normalised z-score for this alignment was 4.4, clearing the benchmark of 2.5 for a good alignment.

The interface between the IR and IGF1R is predicted to form between the β-sheet of the L2 domain and the second (C-terminal) β-sheet and loop regions of the FnIII-1 domains of each monomer respectively (Fig. 1A, B). However, due to the differences in sequence of the IR and IGF1R chains in this region, the interactions are not truly conserved at the contacts between IR L2 and the IGF1R FnIII-1, and *vice versa*. The predicted L2:FnIII-1 interface is structurally similar to the analogous L2: FnIII-1 interfaces of the IR [48] and IGF1R [47] unliganded ectodomain structures, with RMSD values of 1.149 Å and 0.832 Å relative to the relevant regions of the IGF1R (5U8R) and IR (4ZXB), respectively (Supplemental Fig. 3). Analysis of the TACOS model using PDBePISA [54,55] determined that the hybrid L2: FnIII-1 interface covers an area of 1491.1 $Å^2$, with a ΔG (Gibbs free energy) of −5.4 $kcalmol^{-1}$. Typical PPIs exhibit interface areas ranging from 1300 to 2500 $Å^2$ and free energies between −6 and − 12 kcal mol^{-1} [56], meaning the hybrid L2: FnIII-1 interface is both smaller and lower affinity than a typical PPI.

More recently, the development of AlphaFold-multimer [41,57] for protein structure prediction provided an opportunity to further improve the homology model of the IR-IGF1R hybrid receptor. To allow direct comparison to the TACOS model, the sequences corresponding to residues 332–619 of the IR-B and 331–608 of the IGF1R sequences were modelled (Fig. 1 C&D). The model predicted by AlphaFold showed good agreement to the TACOS model with an RMSD of 0.862 Å. Specifically, the secondary structure elements comprising the FnIII-1: L2 interface were highly concurrent, whilst the areas of lower agreement were typically located on the flexible loop regions of the FnIII-1 β-sheets. As the loop regions of the FnIII-1 β-sheets are lower resolution in the template crystal structures and likely highly flexible, discrepancies in modelling of these regions are not particularly concerning.

3.2. Homology model validation

One limitation of the TACOS modelling methodology is the absence of integrated tools for assessing the quality of the generated models. Therefore, the SWISS-MODEL structure assessment suite [58] was utilised to evaluate the TACOS model. QMEANDisCO [43] score was used as the primary metric of assessment generating scores for both global and local quality evaluating the consistency of pairwise Cα- Cα distances in the model by comparing them against restraints extracted from homologous structures allowing comparison of the model to an ensemble of experimental structures. The score is calibrated between 1 and 0, with

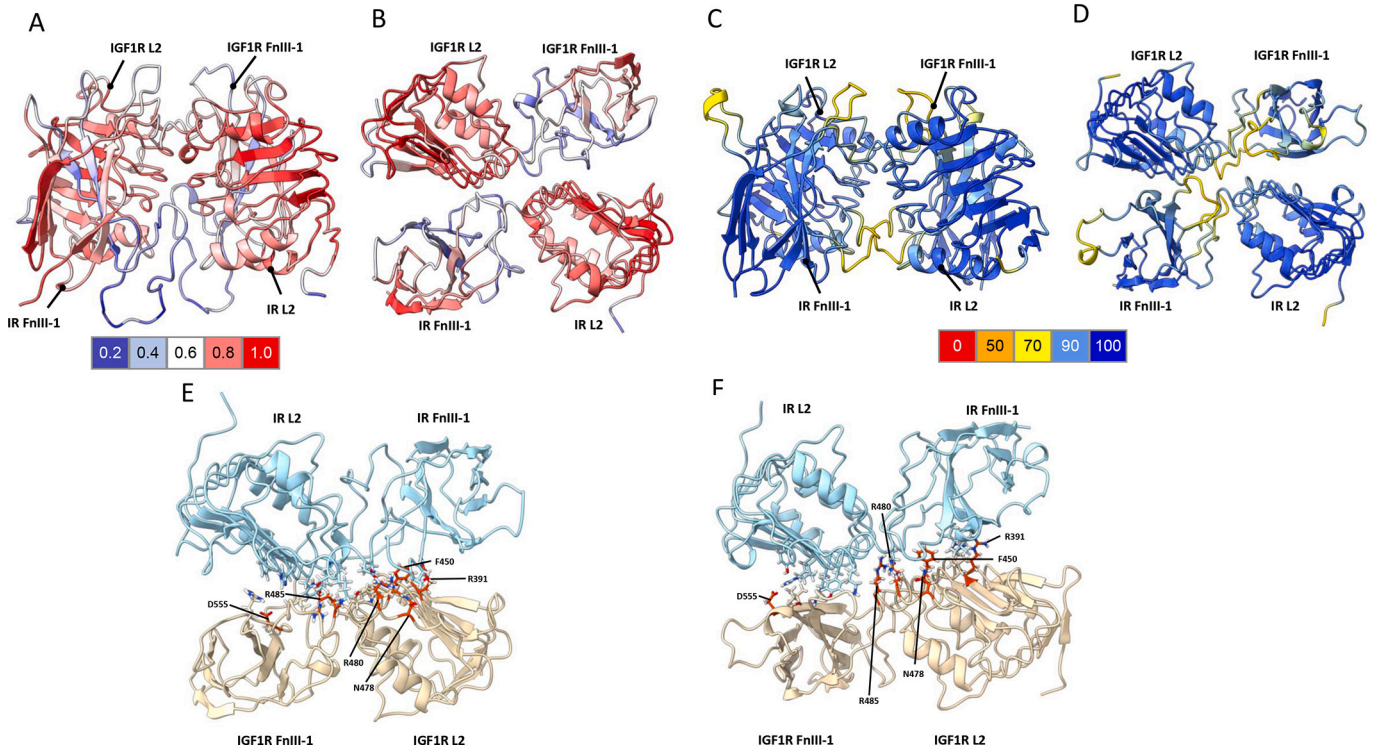

Fig. 1. Homology models of the IR-IGF1R L2: FnIII-1 interface. A) Face-on view of the TACOS homology model coloured by QMEANDisCO score according to the key (colour key at bottom). The QMEANDisCO score is calibrated between 1 and 0, with higher scores indicating higher confidence in the prediction. B) Top-down view of the TACOS homology model coloured by QMEANDisCO score (colour key at bottom). C) Face on view of the Alpha fold homology model with the ribbon coloured by pLDDT (colour key at bottom). D) Top-down view of the AlphaFold homology with ribbon coloured by pLDDT (colour key at bottom). E) KFC2 hotspot analysis of the Hybrid L2: FnIII-1 interface for the TACOS homology model with IR shown as cyan ribbons and IGF1R as wheat-coloured ribbons. Hotspot residues are displayed, with the IGF1R residues which were subsequently mutated in red. F) KFC2 hotspot analysis of the Hybrid L2: FnIII-1 interface for the Alphafold homology model with IR shown as cyan ribbons and IGF1R as wheat-coloured ribbons. Hotspot residues are displayed, with the IGF1R residues which were subsequently mutated in red. (For interpretation of the references to colour in this figure legend, the reader is referred to the web version of this article.)

higher scores indicating higher confidence in the prediction.

The TACOS global QMEANDisCO score was calculated as 0.74 ± 0.05. Additionally, QMEANDisCO per residue analysis was utilised (Supplemental Fig. 1) to assess the local quality relative to the overall model quality. Areas of significantly reduced local quality were identified at IR residues 533–554 and 581–594, as well as in IGF1R residues 544–566 and 599–614. These regions correspond to the β5 strand, β6 strand and connecting loop in the FnIII-1 domains. The lower quality of these regions is unsurprising, as these regions are relatively low resolution in both the template crystal structures. Additionally, a Ramachandran plot (Supplemental Fig. 1) determined that 92.11% residues exhibited favoured dihedral angles, with 0.72% outliers. Overall, assessment metrics for the model indicated it was of good quality [43,58,59], with specific regions in the FnIII-1 domain predicted to be of lower quality.

AlphaFold provides some additional metrics indicating the quality of regions of the predicted model. Firstly, AlphaFold calculates the predicted local distance difference test (pLDDT) which evaluates how well the environment in a reference structure is reproduced in a protein model through comparison of Cα local difference distance tests. The pLDDT score is scaled between 0 and 100, with higher scores indicating higher confidence in the prediction. The pLDDT for the AlphaFold model is generally high (Fig. 1 C&D), with scores <70 isolated to the inter-domain linker regions and flexible loops on the edges of the FnIII-1 domain. AlphaFold also produces a predicted aligned error (PAE)- a measure of the confidence in the relative positioning and orientation of domains in the AlphaFold prediction. The PAE for the AlphaFold model is generally lower than 10 Å (Supplemental Fig. 2), indicating the confidence in the relative positions of the domains is high.

To allow direct comparison with the TACOS model, the AlphaFold model was also evaluated with the SWISS-MODEL structure assessment suite [58]. The AlphaFold model demonstrated a global QMEANDisCO score for the model was 0.78 ± 0.05, indicating a slight improvement compared to the TACOS model (Supplemental Fig. 2). Consistent with the pLDDT score, per residue QMEANDisCO analysis identified lower quality regions of the FnIII-1 domains in both the IR and IGF1R domains. Importantly, these regions were confined to the same loop regions identified by the pLDDT score. This implies that the β5 and β6 strands comprising the core of FnIII-1 domain are predicted with significantly higher confidence in the AlphaFold model relative to the corresponding region of the TACOS model.

Ramachandran analysis of the AlphaFold model determined 96.29% residues occupied favoured conformations, with 0.53% outliers (Supplemental Fig. 2). In comparison, the corresponding values for the TACOS model were 92.11% and 0.72% respectively. Overall, assessment of the AlphaFold and TACOS model indicates that the AlphaFold shows a modest improvement in structural quality, particularly in the β5 and β6 strands of the FnIII-1 domains.

3.3. Prediction of key protein-protein interaction sites in hybrids

Whilst PPI interfaces usually comprise a large area compared to a typical small-molecule binding pocket in a protein, it is accepted that a relatively small-number of amino acid residues contribute a large percentage of the total ΔG^f of a PPI interface [60]. Clusters of such residues are termed 'hotspots'. The KFC2 server [46,61,62] was chosen to computationally predict hotspot residues at the L2: FnIII-1 interface of the TACOS model.

KFC2 hotspot analysis of the Hybrid L2: FnIII-1 interface classified a total of 27 residues as hotspots (Supplemental Table 1) which clustered at the top of the L2 domains of both chains (Fig. 1E) with the interface formation largely governed by hydrophobic interactions, with no hydrogen bonds occurring between hotspot residues from either chain. In the mature hybrid receptor, the IR and IGF1R monomers are held together by intermolecular disulfide bonds, and the dominance of hydrophobic interactions at the L2:FnII-1 interface is consistent with that of many obligate PPI's [63]. Specifically, residues IR Y457 and IGF1R F450 insert into hydrophobic cavities on the opposite monomer, forming critical reciprocal interactions. A further key cluster of contacts occurs where residues IR K487, T488, D491 and Q492 pack against IGF1R residues N478, R480, E484 and R485. IGF1R residues D555 and S522 pack against a cluster of positively charged residues including IR R398 and R399. The number and relative proximities of the predicted hotpot residues was encouraging in terms of disrupting hybrid formation, as they formed compact, well-defined regions.

KFC2 hotspot prediction server was utilised to predict hotspot residues of the AlphaFold homology model. The KFC2a analysis predicted nine IR and nine IGF1R residues as hotspots respectively (Supplemental Table 2). These residues are clustered towards the top of L2 and FnIII-1 domains (Fig. 1F), forming relatively localised epitopes.

The interactions mediated by the hotspot residues exhibit a degree of symmetry between the two receptor chains, although specific interactions are not always conserved. For instance, IR Y457 and IGF1R F450 establish reciprocal interactions by inserting into hydrophobic regions between the L2 and FnIII-1 domains. Similarly, both IR R398 and R399, as well as IGF1R R391 and H392 insert into charged grooves on the opposite FnIII-1 monomer to form electrostatic interactions. IR residues R398 and R399 insert into a negatively charged pocket including IGF1R residues S522 and D555, whilst IGF1R residues R391 and H392 similarly insert into a negatively charged cluster on the IR, contacting IR F530 and L596. Additionally, both IR L196 and IGF1R I295 are involved in packing against hydrophobic regions on the opposite monomer.

Three hotspot residues from each chain were predicted by KFC2 for both the TACOS and AlphaFold model. These residues include IR Y457, IR K487, IR Q492, IGF1R F450, IGF1R N478 and IGF1R R485, which are all contained in the L2 domain. It is notable that there are discrepancies in the hotspot residues predicted within the FnIII-1 domains. This disparity can likely be attributed to reduced quality of this region in the TACOS model, indicating that the FnIII-1 residues predicted by the AlphaFold model should be prioritised over those from the TACOS model. The contrasting predictions of hotspot residues between the AlphaFold and TACOS models highlights the variations in local structural details despite the high RMSD indicating good overall agreement between the two models. This reinforces the importance of considering multiple modelling approaches and prioritising regions of higher confidence when utilising results obtained from homology models.

To investigate their potential functional significance, hotspot residues identified by KFC2 were compared with the Human Gene Mutation Database [64], to determine if these residues had previously been identified as disease-causing mutations. Notably, the two point mutations IR K487E [65], T488P [66] have been documented as natural disease-causing variants associated with Donohue Syndrome. This disease is characterised by severe insulin resistance and significant growth restriction in humans, implying these residues have significant functional importance.

Evaluation of Predicted Hotspots Using Site-Directed Mutagenesis.

To experimentally validate the hotspot residues identified using the KFC2 server [46], site directed mutagenesis was employed to generate a series of chimeric IR-IGF1R receptors containing point mutations at selected hotspot residues. Alanine mutations were chosen as they represent the truncation of the amino acid side chain to the β-carbon, whilst retaining the backbone dihedral angle preferences of most amino acids. These mutant receptors could then be characterised biochemically to determine the importance of each mutation to the IR-IGF1R PPI.

Mutagenesis was performed cDNAs encoding the IR fused to *Renilla Luciferase* (IR-Rluc) and IGF1R fused to second generation yellow fluorescent protein (IGF1R-YPET), to allow detection of IR-IGF1R hybrid protein. Mutants were generated by a PCR-based approach involving the amplification of the IR-Rluc and IGF1R-YPET plasmids (Supplemental Fig. 4) utilising Platinum SuperFi II polymerase, which amplified IR-Rluc and IGF1R-YPET vectors more specifically at a universal

annealing temperature of 60 °C (Fig. 2A). The IGF1R gene was sequenced to ensure the desired mutations had been incorporated and no additional mutations had been erroneously generated during PCR (Supplemental Fig. 5).

3.4. Functional evaluation of hybrid receptor constructs

Once the mutated plasmid sequences had been verified, functional analysis of the resulting mutants was carried out. The ability of the mutant receptors to be transported in the cell membrane was evaluated by fluorescence microscopy, which detected the YPET labelled IGF1R hemireceptor (Supplemental Fig. 6). This experiment confirmed that yellow fluorescence was predominantly located at the cell membrane for wild-type IGF1R-YPET co-transfected into HEK293 cells with IR-Rluc. Similarly, each of the mutant receptor construct displayed fluorescence localised to the cell membrane when co-transfected with IR-Rluc. This contrasted to YPET transfected alone, in which high levels of fluorescence could be detected in the cell cytoplasm. Additionally, western blotting was utilised to ensure the mutant receptors were phosphorylated in response to IGF1 stimulation, indicating that they are functional (Supplemental Fig. 7). Whilst this assay will also detect an IGF1R homomeric component, the presence of the mutant IGF1R constructs did not alter this signalling when compared to the signalling of the wild-type receptor. With confirmation that the mutated receptors did not show altered signalling or subcellular localisation, the effect of the mutations on the receptor binding interface could be evaluated.

To evaluate the effect of the incorporated mutations on hybrid formation, a cell-based bioluminescence resonance energy transfer screening assay based on the system previously described by Blanqaurt *et. al* [67] was utilised. This assay was used to monitor the interaction between IR-Rluc and IGF1R-YPET in the hybrid receptors. The fluorescence of YPET is dependent on a resonance energy transfer interaction between the *Rluc* and YPET tags when in proximity and the presence of the *Rluc* substrate coloenterazine-h. The BRET assay can differentiate between homo and heteromeric receptors, as only hybrid receptors containing both the Rluc and YPET tags are BRET competent. BRET signal is expressed as a ratio of the signal corresponding to the luminescence of *Rluc* at 485 nm and the luminescence of YPET at 535 nm. To account for the spectral overlap of Rluc and YPET luminescence, the background signal is determined by transfecting the *Rluc* tagged receptor alone. This is used to determine the background luminescence ratio between 485 nm and 535 nm and subtracting this from the BRET ratio calculated for both partners (Supplemental Fig. 8).

The specificity of the BRET interaction between the IR-Rluc and IGF1R-YPET (WT) constructs was confirmed by a donor-saturation assay, in which the ratio of the BRET acceptor (IGF1R-YPET) was varied relative to the BRET donor (Fig. 2B). The hyperbolic increase in BRET signal with increasing acceptor/donor ratio is typical of a specific BRET interaction, with the final plateau representing the saturation of all donor molecules.

To obtain receptor/donor ratios that equate to real protein quantities in the donor saturation assay, luciferase and YPET fluorescence must be correlated to receptor numbers to allow conversion. Receptor numbers for the IR-Rluc and IGF1R-YPET constructs were determined by a radioligand saturation binding assay. Cells were transfected with increasing quantities of cDNA encoding IR-Rluc or IGF1R-YPET. Subsequently, the luminescence and fluorescence values corresponding to IR-Rluc in the presence of 5 μM coelenterazine or YPET excited at 513 nm were determined for each transfection. Cells expressing the chimeric receptors were then probed with increasing concentrations of ^{125}I-Insulin or ^{125}I-IGF1 before bound probes were recorded. Non-specific binding was also evaluated by incubating cells with ^{125}I-Insulin or ^{125}I-IGFI in the presence of unlabelled insulin or IGFI at 500 nM to block specific binding (Fig. 2 C&E). From these assays, the K_d for the IR-Rluc and IGF1R-YPET constructs were determined as 140 ± 25.2 pM and 122.8 ± 24.2 pM, which are in good accordance with the apparent K_d values of 190 pM and 120 pM reported [68] for the IR and IGF1R respectively. It is noted in the case of IR-Rluc, the K_d value may be altered by the presence of the fused Rluc tag.

The B_{max} values for each transfection ratio were found to vary

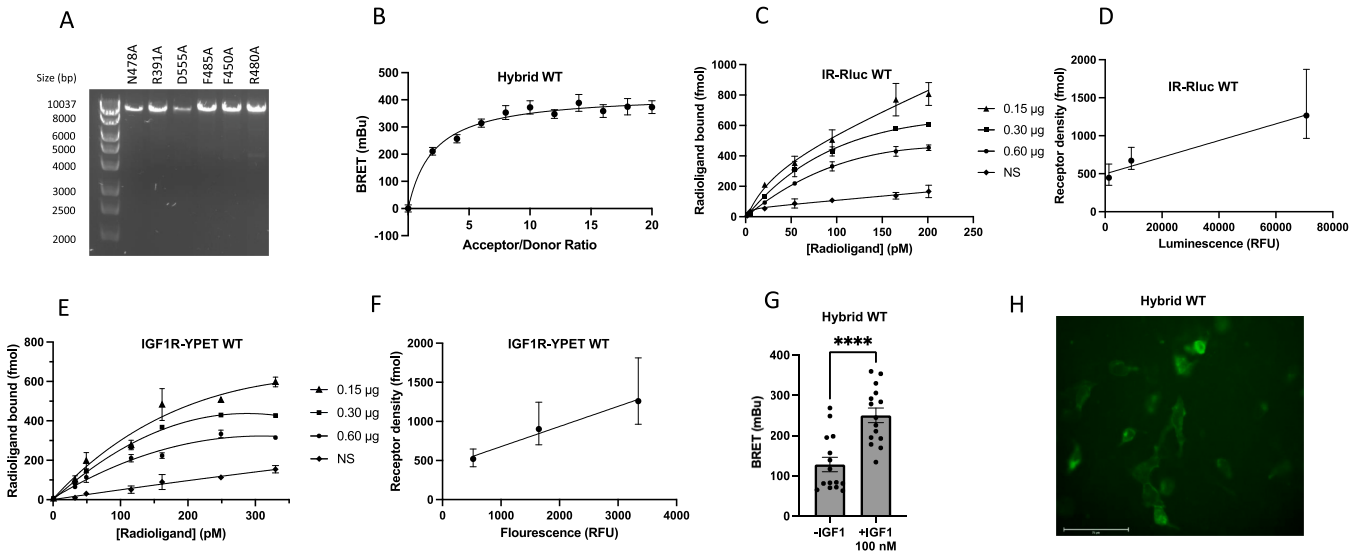

Fig. 2. Radioligand binding assays to determine how IR-Rluc and IGF1R-YPET (WT) receptor quantities are correlated with their relative luminescence and fluorescence, respectively. A) PCR product when PCR was performed using SuperFi II Platinum mastermix. B) Donor saturation assay curve for BRET constructs WT IR-Rluc and WT IGF1R-YPET, where WT IR-Rluc is saturated with increasing WT IGF1R-YPET (±SEM). C) Saturation radioligand bind curves for the WT IR-Rluc constructs with ^{125}I insulin tracer. The key indicates the amount of DNA per transfection used in each experiment. The NS curve depicts the non-specific binding component determined for untransfected cells ($n = 2$; ± SEM. D) Calibration of WT IR-Rluc luminescence in the presence of 5 μM coelenterazine to receptor numbers (± SEM) E) Saturation radioligand bind curves for the WT IGF1R-YPET constructs with ^{125}I IGF1 tracer. The key indicates the amount of DNA per transfection used in each experiment. The NS line depicts the non-specific binding component determined for untransfected cells (n = 2; ± SEM) F) Calibration of WT IGF1R fluorescence when excited at 513 nm to total receptor numbers (± SEM). G) BRET measurements showing the effect of treating cells co-transfected with WT IR-Rluc and WT IGF1R-YPET with IGF1 (100 nM, 5 min treatment, $n = 8,2$; $p < 0.0001$ ± SEM). H) Representative fluorescence microscopy images of HEK293 cells transfected with WT IR-Rluc and WT IGF1R-YPET, indicating the subcellar location of YPET, scale bar = 75 μm.

linearly with luminescence and fluorescence values for the IR-Rluc and IGF1R-YPET constructs respectively (Fig. 2 D&F). This in turn allows the conversion between luminescence, fluorescence values and actual protein quantities for the IR-Rluc and IGF1R-YPET constructs respectively. It was reasonable to assume that point mutations in the receptor ectodomains would not affect luminescence and fluorescence originating from the C-terminal Rluc and YPET tags. Therefore, this analysis could similarly be utilised to convert between luminescence, fluorescence, and actual protein quantities for the chimeric mutant receptors.

Additionally, in cells transfected with IR-Rluc and IGF1R-YPET, an enhanced BRET signal could be observed upon stimulation with 100 nM of IGF1 (Fig. 2G). This BRET increase was comparable in magnitude to that previously reported in hybrid receptors similarly tagged with Rluc and YPET [67]. Finally, the subcellar location of the chimeric IR-IGF1R hybrid receptors was assessed to ensure they were correctly trafficked to the cell membrane. Using fluorescence microscopy, YPET signal was observed localised to the cell membrane in HEK293 cells co-transfected with IR-Rluc and IGF1R-YPET (Fig. 2H). This result confirms that the attachment of BRET tags has not hindered the robust processing and trafficking of the chimeric hybrid receptors.

3.5. Donor saturation assays to characterise hybrid receptor mutants

Donor saturation assays were undertaken by co-transfection of WT-IR-Rluc and mutant IGF1R-YPET, incorporating mutant IGF1R-YPET as part of a hybrid receptor. A non-linear regression model was used to fit to the data and calculate $BRET_{50}$ and $BRET_{max}$ values. The donor saturation assays determined that mutation of IGF1R residues F450A (Fig. 3A), R391A (Fig. 3B) and D555A (Fig. 3C) did reduce the affinity of the IR IGF1R complex, as these mutants showed increased $BRET_{50}$ values in the assay relative to the value for the hybrid WT receptor (Fig. 3G). This result implies that each of these residues plays a significant role in stabilising the IR- IGF1R L2 FnIII-1 interface.

IGF1R residue F450 was predicted as a hotspot residue in both the AlphaFold and TACOS models (Fig. 4A). In both models, the phenylalanine side chain inserts into a hydrophobic pocket on the IR monomer, stabilising the interface through hydrophobic interactions. Mutation of phenylalanine to alanine represents removal of the phenyl ring, which likely results in reduced hydrophobic contact and diminished interaction strength between the hybrid monomers. Noticeably, the mutant receptor also shows a substantial increase in $BRET_{max}$ relative to the wild-type receptor, indicating that the mutation results in a change in the receptor conformation. As the $BRET_{50}$ measurement is proportional to $BRET_{max}$, the change in $BRET_{50}$ cannot definitively be attributed to a change in IR and IGF1R affinity and may be due to the inherent relationship between the two parameters. Conversely, a change in receptor affinity could be affected by a large-scale conformational change of the receptor facilitated by the mutation F450A, which may explain the two-fold change in $BRET_{50}$ from the point mutation of a single residue. It is notable that no change in subcellular location or signalling in response to IGF1 treatment was observed with this receptor. Therefore, any conformational change occurring due to the F450A mutation does not appear to substantially alter the receptors processing or signalling properties.

The residue R391 was predicted as a hotspot residue by the AlphaFold model and extends into a positively charged pocket on the IR monomer to form electrostatic interactions with surrounding residues (Fig. 4B). Mutation to alanine results in the removal of electrostatic interactions and steric bulk and therefore reduce the affinity with the IR monomer. Similarly, residue D555 was predicted as a hotspot residue on by the AlphaFold model (Fig. 4C). This residue extends to form electrostatic interactions with a cluster of residues positively charged residues located on the IR monomer. Mutation to alanine would result in the removal of these electrostatic interactions. Both mutations show no significant change in $BRET_{max}$ relative to the wild-type receptor, meaning that the change in $BRET_{50}$ can be interpreted as a change in the receptor affinity upon mutation of the receptor.

The residues R480, R485 and N478 were similarly predicted as hotspot residues. However, there was no significant deviation in $BRET_{50}$ observed with these mutants relative to the wild-type (Fig. 3D-G). It is possible that these were hotspots, but the donor saturation assay was not sensitive enough to detect changes in affinity caused by these mutations.

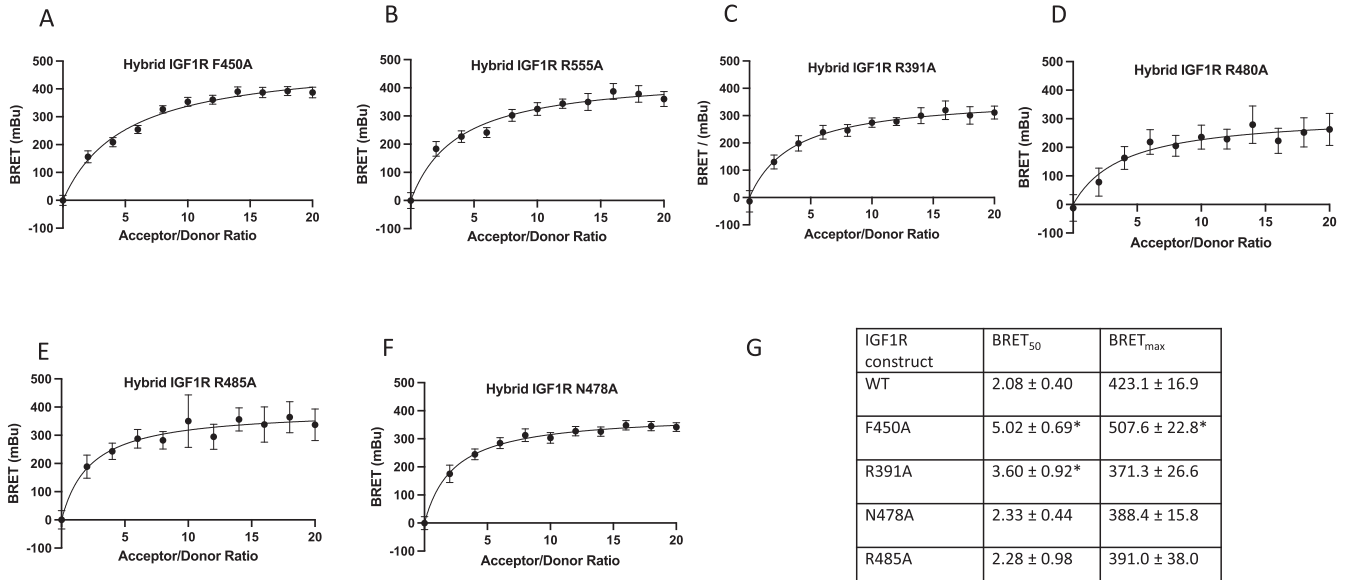

G

IGF1R construct	$BRET_{50}$	$BRET_{max}$
WT	2.08 ± 0.40	423.1 ± 16.9
F450A	5.02 ± 0.69*	507.6 ± 22.8*
R391A	3.60 ± 0.92*	371.3 ± 26.6
N478A	2.33 ± 0.44	388.4 ± 15.8
R485A	2.28 ± 0.98	391.0 ± 38.0
D555A	3.74 ± 0.80*	446.5 ± 27.0
R480A	3.95 ± 1.75	316.1 ± 43.2

Fig. 3. $BRET_{max}$ and $BRET_{50}$ parameters determined for each of the IR-IGF1R hybrid mutants in the donor saturation assay. A-F) Representative donor saturation assay curves performed for IR-IGF1R-hybrid mutants (n = 8; ± SEM). G) $BRET_{50}$ and $BRET_{max}$ parameters determined for each of the IR-IGF1R hybrid mutants in the donor saturation assay. Error ranges represent the 95% confidence interval determined for the non-linear regression curve calculated from three separate experiments (n = 8,3). *$p < 0.05$ when compared to WT.

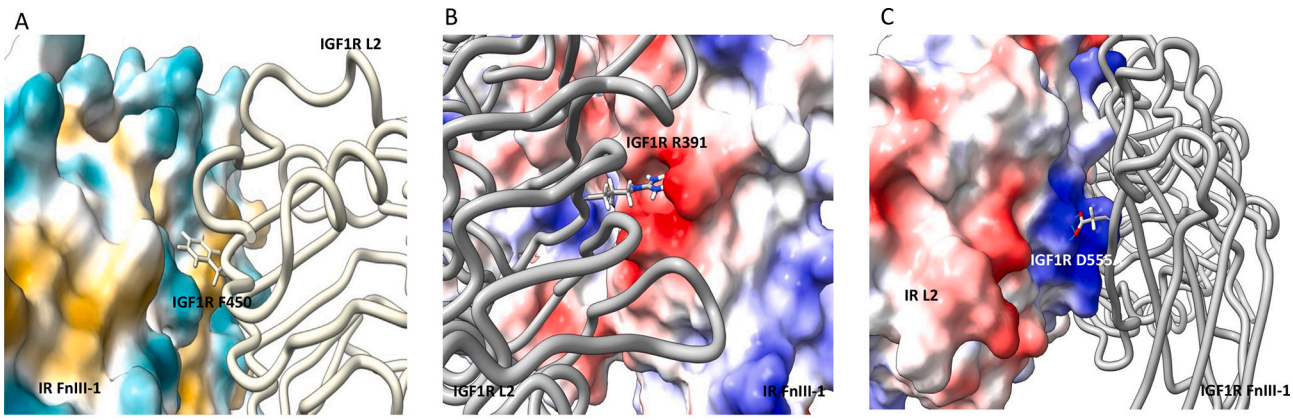

D

```
IGF1R_HUMAN LQGCTIFKGNLLINIRRGNNIASELENFMGLIEVVTGYVKIRHSHALVSLSFLKNLRLIL 409
INSR_HUMAN  LRGCTVINGSLIINIRGGNNLAAELEANLGLIEEISGYLKIRRSYALVSLSFFRKLRLIR 416
            *:***:::*.*:**** ***:*:***  :**** ::**:***:*:*******:::**** 
IGF1R_HUMAN GEEQLEGNYSFYVLDNQNLQQLWDWDHRNLTIKAGKMYFAFNPKLCVSEIYRMEEVTGTK 469
INSR_HUMAN  GETLEIGNYSFYALDNQNLRQLWDWSKHNLTITQGKLFFHYNPKLCLSEIHKMEEVSGTK 476
            **     ******.******:*****.::****. **::* :*****:***::****:*** 
IGF1R_HUMAN GRQSKGDINTRNNGERASCESDVLHFTSTTTSKNRIIITWHRYRPPDYRDLISFTVYYKE 529
INSR_HUMAN  GRQERNDIALKTNGDQASCENELLKFSYIRTSFDKILLRWEPYWPPDFRDLLGFMLFYKE 536
            ***.:.**  :.**::****.::*:*:   ** ::*:: *. * ***:***:.* ::*** 
IGF1R_HUMAN APFKNVTEYDGQDACGSNSWNMVDVDLPP-----NKDVEPGILLHGLKPWTQYAVYVKAV 584
INSR_HUMAN  APYQNVTEFDGQDACGSNSWTVVDIDPPLRSNDPKSQNHPGWLMRGLKPWTQYAIFVKTL 596
            **::****:**********.:**:* *       :.: .** *::*********::***: 
IGF1R_HUMAN TLTMVENDHIRGAKSEILYIRTNASVPSIPLDVLSASNSSSQLIVKWNPPSLPNGNLSYY 644
INSR_HUMAN  V-TFSDERRTYGAKSDIIYVQTDATNPSVPLDPISVSNSSSQIILKWKPPSDPNGNITHY 655
            . *: :: :  ****:*:*::*:*: **:*** :*.******:*:**:*** ****:::*
```

Fig. 4. Predicted interactions of the IGF1R residues for which mutation to alanine cause an increase in $BRET_{50}$. All images are taken from the AlphaFold homology model. A) Interaction of IGF1R F450 with the IR. The IGF1R is shown in yellow and IR with surface coloured by hydrophobicity; B) The interaction of IGF1R R391 with the IR. The IGF1R is shown in grey and IR with an electrostatic surface; C) The interaction of D555 with the IR. The IGF1R is shown in grey and IR with and electrostatic surface. D) Sequence alignment of the IR and IGF1R FnIII-1/L2 domains. The IGF1R residues mutated in this study have been highlighted in bold. Residues predicted as hotspots in the TACOS mode (red), AlphaFold model (blue) and both models (green) are also highlighted. Below the protein sequences is a key denoting conserved sequence (*), conservative mutations (:), semi-conservative mutations (.), and non-conservative mutations (). (For interpretation of the references to colour in this figure legend, the reader is referred to the web version of this article.)

The capacity for IGF1R residues R391 and D555A to modulate the affinity of the hybrid receptor suggests these amino acids, and their equivalent IR residues, may be important in the formation of IGF1R and IR homodimers. An alignment of the IR and IGF1R L2/FnIII-1 sequences reveals that IGF1R R391 and D555A are fully conserved in the IR, equivalent to R398 and D562 respectively (Fig. 4D). Similarly, IGF1R F450, which was also identified in this study, is conservatively replaced by IR Y457. This is likely due to the selective pressure to conserve residues important for receptor dimerisation. Of the residues experimentally examined in this study, only N478 was completely non-conserved between the IR and IGF1R, and we did not observe a significant perturbation in heterodimer affinity in the N478A mutant relative to the wild-type receptor. Therefore, in terms of modulating receptor formation for therapeutic intervention, it will be important to exploit the differences in local amino acids surrounding the hotspot residues to selectively modulate hybrid formation, as the hotspot residues identified in this study appear to be relatively well conserved.

The ability of residues IGF1R R391 and D555A to alter the apparent affinity of the hybrid receptor is significant, as it confirms that hybrid receptor formation can be modulated pre-dimerisation by changes to residues at the L2: FnIII-1 interface. Once the receptors are dimerised, the formation of disulfide bonds effectively locks their dimeric arrangement [69]. Whilst mutations to residues at the L2:FnIII-1 interface are unlikely to be the major cause of IR-IGF1R upregulation in response to metabolic disease [33], the fact that receptor dimerisation can be modulated by this confirms epitopes at the L2:FnIII-1 interface are a suitable target for therapeutic intervention.

4. Conclusions

Two homology models of the IR-IG1F1R hybrid ectodomain were generated utilising TACOS and AlphaFold Multimer. These methodologies have independently predicted the formation of an interface between the L2 and FnIII-1 domains in the hybrid receptor. This interface was evaluated by SiteMap and KFC2, identifying suitable drug-binding regions and hotspot residues for small molecule intervention. Six IGF1R receptor mutants have been generated and their ability to disrupt hybrid formation has been assessed. All the generated mutants were expressed robustly, and the chimeric receptors IGF1R F450A, R391A and D555A all showed reduced affinity as part of a hybrid receptor.

There has been great progress in recent years towards the understanding of IR, IGF1R and hybrid structure and the conformational changes from apo to ligand bound receptors [34,48,70,71]. In lieu of any current structural information regarding hybrid receptor apo structure, this work goes some way to understand the key hotspots for hybrid receptor dimerisation. This shows for the first time that hybrid receptor formation can be manipulated at the protein level and highlights the importance of the L2: FnIII-1 interface in controlling hybrid receptor dimerisation. All the receptor mutants that showed reduced $BRET_{50}$ relative to the wild-type receptor were predicted by the KFC2b method on the AlphaFold homology model, implying that this model can be used to predict hotspot features at the L2: FnIII-1 interface with good accuracy.

A limitation of this approach is that the large size of the IR-IGF1R hybrid receptor precluded modelling of the entire receptor. Whilst it is likely that interactions between individual receptor domains is somewhat independent from the entire receptor, a complete model of the receptor would be preferable. It was also notable that the AlphaFold and TACOS models showed limited agreement on the identity of hotspot residues when evaluated by KFC2.

Funding

This work was supported by the British Heart Foundation-grant number FS/19/59/34896.

CRediT authorship contribution statement

Samuel Turvey: Writing – review & editing, Writing – original draft, Methodology, Investigation, Formal analysis, Data curation, Conceptualization. **Stephen P. Muench:** Writing – review & editing, Supervision, Conceptualization. **Tarik Issad:** Writing – review & editing, Resources. **Colin W.G. Fishwick:** Supervision. **Mark T. Kearney:** Writing – review & editing, Resources, Funding acquisition. **Katie J. Simmons:** Writing – review & editing, Writing – original draft, Supervision, Investigation, Conceptualization.

Declaration of competing interest

The authors declare that they have no competing interests.

Appendix A. Supplementary data

Supplementary data to this article can be found online at https://doi.org/10.1016/j.ghir.2024.101607.

References

[1] B.A. Swinburn, G. Sacks, K.D. Hall, K. McPherson, D.T. Finegood, M.L. Moodie, S. L. Gortmaker, The global obesity pandemic: shaped by global drivers and local environments, Lancet 378 (9793) (2011) 804–814.
[2] L. Guariguata, D.R. Whiting, I. Hambleton, J. Beagley, U. Linnenkamp, J.E. Shaw, Global estimates of diabetes prevalence for 2013 and projections for 2035, Diabetes Res. Clin. Pract. 103 (2) (2014) 137–149.
[3] M.C. Petersen, G.I. Shulman, Mechanisms of insulin action and insulin resistance, Physiol. Rev. 98 (4) (2018) 2133–2223.
[4] M. Roden, G.I. Shulman, The integrative biology of type 2 diabetes, Nature 576 (7785) (2019) 51–60.
[5] V.T. Samuel, G.I. Shulman, The pathogenesis of insulin resistance: integrating signaling pathways and substrate flux, J. Clin. Invest. 126 (1) (2016) 12–22.
[6] C.M. Taniguchi, B. Emanuelli, C.R. Kahn, Critical nodes in signalling pathways: insights into insulin action, Nat. Rev. Mol. Cell Biol. 7 (2) (2006) 85–96.
[7] R.S. Garofalo, Genetic analysis of insulin signaling in Drosophila, Trends Endocrinol. Metab. 13 (4) (2002) 156–162.
[8] Kien T. Tan, S.-C. Luo, W.-Z. Ho, Y.-H. Lee, Insulin/IGF-1 receptor signaling enhances biosynthetic activity and fat mobilization in the initial phase of starvation in adult male C. elegans, Cell Metab. 14 (3) (2011) 390–402.
[9] A. Belfiore, F. Frasca, G. Pandini, L. Sciacca, R. Vigneri, Insulin receptor isoforms and insulin receptor/insulin-like growth factor receptor hybrids in physiology and disease, Endocr. Rev. 30 (6) (2009) 586–623.
[10] B.D. Manning, L.C. Cantley, AKT/PKB signaling: navigating downstream, Cell 129 (7) (2007) 1261–1274.
[11] S. Dimmeler, I. Fleming, B. Fisslthaler, C. Hermann, R. Busse, A.M. Zeiher, Activation of nitric oxide synthase in endothelial cells by Akt-dependent phosphorylation, Nature 399 (6736) (1999) 601–605.
[12] D. Fulton, J.P. Gratton, T.J. McCabe, J. Fontana, Y. Fujio, K. Walsh, T.F. Franke, A. Papapetropoulos, W.C. Sessa, Regulation of endothelium-derived nitric oxide production by the protein kinase Akt, Nature 399 (6736) (1999) 597–601.
[13] W. Cai, M. Sakaguchi, A. Kleinridders, G. Gonzalez-Del Pino, J.M. Dreyfuss, B. T. O'Neill, A.K. Ramirez, H. Pan, J.N. Winnay, J. Boucher, M.J. Eck, C.R. Kahn, Domain-dependent effects of insulin and IGF-1 receptors on signalling and gene expression, Nat. Commun. 8 (2017) 14892.
[14] E.R. Duncan, S.J. Walker, V.A. Ezzat, S.B. Wheatcroft, J.M. Li, A.M. Shah, M. T. Kearney, Accelerated endothelial dysfunction in mild prediabetic insulin resistance: the early role of reactive oxygen species, American journal of physiology, Endocrinol. Metab. 293 (5) (2007) E1311–E1319.
[15] P. Sukumar, H. Viswambharan, H. Imrie, R.M. Cubbon, N. Yuldasheva, M. Gage, S. Galloway, A. Skromna, P. Kandavelu, C.X. Santos, V.K. Gatenby, J. Smith, D. J. Beech, S.B. Wheatcroft, K.M. Channon, A.M. Shah, M.T. Kearney, Nox2 NADPH oxidase has a critical role in insulin resistance–related endothelial cell dysfunction, Diabetes 62 (6) (2013) 2130–2134.
[16] A. Abbas, H. Imrie, H. Viswambharan, P. Sukumar, A. Rajwani, R.M. Cubbon, M. Gage, J. Smith, S. Galloway, N. Yuldeshava, M. Kahn, S. Xuan, P.J. Grant, K. M. Channon, D.J. Beech, S.B. Wheatcroft, M.T. Kearney, The insulin-like growth Factor-1 receptor is a negative regulator of nitric oxide bioavailability and insulin sensitivity in the endothelium, Diabetes 60 (8) (2011) 2169–2178.
[17] H. Viswambharan, N.Y. Yuldasheva, A. Sengupta, H. Imrie, M.C. Gage, N. Haywood, A.M.N. Walker, A. Skromna, N. Makova, S. Galloway, P. Shah, P. Sukumar, K.E. Porter, P.J. Grant, A.M. Shah, C.X.C. Santos, J. Li, D.J. Beech, S. B. Wheatcroft, R.M. Cubbon, M.T. Kearney, Selective enhancement of insulin sensitivity in the endothelium in vivo reveals a novel Proatherosclerotic signaling loop, Circ. Res. 120 (5) (2017) 784–798.
[18] H. Imrie, H. Viswambharan, P. Sukumar, A. Abbas, R.M. Cubbon, N. Yuldasheva, M. Gage, J. Smith, S. Galloway, A. Skromna, S.T. Rashid, T.S. Futers, S. Xuan, V. K. Gatenby, P.J. Grant, K.M. Channon, D.J. Beech, S.B. Wheatcroft, M.T. Kearney, Novel role of the IGF-1 receptor in endothelial function and repair: studies in endothelium-targeted IGF-1 receptor transgenic mice, Diabetes 61 (9) (2012) 2359–2368.
[19] P. De Meyts, J. Whittaker, Structural biology of insulin and IGF1 receptors: implications for drug design, Nat. Rev. Drug Discov. 1 (10) (2002) 769–783.
[20] S.T. Henderson, G.V. Brierley, K.H. Surinya, I.K. Priebe, D.E.A. Catcheside, J. C. Wallace, B.E. Forbes, L.J. Cosgrove, Delineation of the IGF-II C domain elements involved in binding and activation of the IR-A, IR-B and IGF-IR, Growth Hormon. IGF Res. 25 (1) (2015) 20–27.
[21] G. Pandini, F. Frasca, R. Mineo, L. Sciacca, R. Vigneri, A. Belfiore, Insulin/insulin-like growth factor I hybrid receptors have different biological characteristics depending on the insulin receptor isoform involved, J. Biol. Chem. 277 (42) (2002) 39684–39695.
[22] R. Slaaby, Hybrid receptors formed by Insulin Receptor (IR) and insulin-like growth factor I receptor (IGF-IR) have low insulin and high IGF-1 affinity irrespective of the IR splice variant 281 (36) (2006) 25869–25874.
[23] Y. Chen, J. McGee, X. Chen, T.N. Doman, X. Gong, Y. Zhang, N. Hamm, X. Ma, R. E. Higgs, S.V. Bhagwat, S. Buchanan, S.-B. Peng, K.A. Staschke, V. Yadav, Y. Yue, H. Kouros-Mehr, Identification of Druggable Cancer driver genes amplified across TCGA datasets, PLoS One 9 (5) (2014) e98293.
[24] P. De Meyts, Insulin/receptor binding: the last piece of the puzzle? BioEssays 37 (4) (2015) 389–397.
[25] H. Imrie, H. Viswambharan, P. Sukumar, A. Abbas, R.M. Cubbon, N. Yuldasheva, M. Gage, J. Smith, S. Galloway, A. Skromna, S.T. Rashid, T.S. Futers, S. Xuan, V. K. Gatenby, P.J. Grant, K.M. Channon, D.J. Beech, S.B. Wheatcroft, M.T. Kearney, Novel role of the IGF-1 receptor in endothelial function and repair: studies in endothelium-targeted IGF-1 receptor transgenic mice, Diabetes 61 (9) (2012) 2359.
[26] A. Abbas, H. Imrie, H. Viswambharan, P. Sukumar, A. Rajwani, R.M. Cubbon, M. Gage, J. Smith, S. Galloway, N. Yuldeshava, M. Kahn, S. Xuan, P.J. Grant, K. M. Channon, D.J. Beech, S.B. Wheatcroft, M.T. Kearney, The insulin-like growth factor-1 receptor is a negative regulator of nitric oxide bioavailability and insulin sensitivity in the endothelium, Diabetes 60 (8) (2011) 2169–2178.
[27] G. Pandini, R. Vigneri, A. Costantino, F. Frasca, A. Ippolito, Y. Fujita-Yamaguchi, K. Siddle, I.D. Goldfine, A. Belfiore, Insulin and insulin-like growth factor-I (IGF-I) receptor overexpression in breast cancers leads to insulin/IGF-I hybrid receptor overexpression: evidence for a second mechanism of IGF-I signaling, Clin. Cancer Res. 5 (7) (1999) 1935–1944.
[28] E.M. Bailyes, B.T. Navé, M.A. Soos, S.R. Orr, A.C. Hayward, K. Siddle, Insulin receptor/IGF-I receptor hybrids are widely distributed in mammalian tissues: quantification of individual receptor species by selective immunoprecipitation and immunoblotting, Biochem. J. 327 (1) (1997) 209–215.
[29] M. Federici, O. Porzio, L. Zucaro, B. Giovannone, P. Borboni, M.A. Marini, D. Lauro, G. Sesti, Increased abundance of insulin/IGF-I hybrid receptors in adipose tissue from NIDDM patients, Mol. Cell. Endocrinol. 135 (1) (1997) 41–47.
[30] M. Federici, L. Zucaro, O. Porzio, R. Massoud, P. Borboni, D. Lauro, G. Sesti, Increased expression of insulin/insulin-like growth factor-I hybrid receptors in skeletal muscle of noninsulin-dependent diabetes mellitus subjects, J. Clin. Invest. 98 (12) (1996) 2887–2893.
[31] M. Federici, D. Lauro, M. D'Adamo, B. Giovannone, O. Porzio, M. Mellozzi, G. Tamburrano, P. Sbraccia, G. Sesti, Expression of insulin/IGF-I hybrid receptors is increased in skeletal muscle of patients with chronic primary hyperinsulinemia, Diabetes 47 (1) (1998) 87–92.
[32] H. Valensise, Y.Y. Liu, M. Federici, D. Lauro, D. Dell'anna, C. Romanini, G. Sesti, Increased expression of low-affinity insulin receptor isoform and insulin/insulin-like growth factor-I hybrid receptors in term placenta from insulin-resistant women with gestational hypertension, Diabetologia 39 (8) (1996) 952.
[33] M. Federici, A. Giaccari, M.L. Hribal, B. Giovannone, D. Lauro, L. Morviducci, L. Pastore, G. Tamburrano, R. Lauro, G. Sesti, Evidence for glucose/hexosamine in vivo regulation of insulin/IGF-I hybrid receptor assembly, Diabetes 48 (12) (1999) 2277–2285.
[34] Y.B. Xu, M.B. Margetts, H. Venugopal, J.G. Menting, N.S. Kirk, T.I. Croll, C. Delaine, B.E. Forbes, M.C. Lawrence, How insulin-like growth factor I binds to a hybrid insulin receptor type 1 insulin-like growth factor receptor, Structure 30 (8) (2022) 1098.
[35] C.A. Schneider, W.S. Rasband, K.W. Eliceiri, NIH image to ImageJ: 25 years of image analysis, Nat. Methods 9 (7) (2012) 671–675.
[36] S. Bienert, A. Waterhouse, A.P. de Tjaart, G. Beer, G. Tauriello, L. Studer, T. Schwede Bordoli, The SWISS-MODEL repository—new features and functionality, Nucleic Acids Res. 45 (D1) (2016) D313–D319.
[37] C. UniProt, UniProt: the universal protein knowledgebase in 2021, Nucleic Acids Res. 49 (D1) (2021) D480–D489.
[38] T.U. Consortium, UniProt: the universal protein knowledgebase in 2023, Nucleic Acids Res. 51 (D1) (2022) D523–D531.
[39] U. Consortium, UniProt. https://www.uniprot.org/.
[40] M. Mirdita, K. Schütze, Y. Moriwaki, L. Heo, S. Ovchinnikov, M. Steinegger, ColabFold: making protein folding accessible to all, Nat. Methods 19 (6) (2022) 679–682.
[41] R. Evans, M. O'Neill, A. Pritzel, N. Antropova, A. Senior, T. Green, A. Žídek, R. Bates, S. Blackwell, J. Yim, O. Ronneberger, S. Bodenstein, M. Zielinski, A.

Bridgland, A. Potapenko, A. Cowie, K. Tunyasuvunakool, R. Jain, E. Clancy, P. Kohli, J. Jumper, D. Hassabis, Protein complex prediction with AlphaFold-Multimer. bioRxiv 2021.10.04.463034; doi: 10.1101/2021.10.04.463034.
[42] E.F. Pettersen, T.D. Goddard, C.C. Huang, E.C. Meng, G.S. Couch, T.I. Croll, J. H. Morris, T.E. Ferrin, U.C.S.F. ChimeraX, Structure visualization for researchers, educators, and developers, Protein Sci. 30 (1) (2021) 70–82.
[43] G. Studer, C. Rempfer, A.M. Waterhouse, R. Gumienny, J. Haas, T. Schwede, QMEANDisCo-distance constraints applied on model quality estimation, Bioinformatics 36 (6) (2020) 1765–1771.
[44] SWISS-MODEL. https://swissmodel.expasy.org/ (Accessed 13/05/2021).
[45] SWISS-MODEL Structure Assessment. https://swissmodel.expasy.org/ (Accessed 13/05/2021).
[46] X. Zhu, J.C. Mitchell, KFC2: a knowledge-based hot spot prediction method based on interface solvation, atomic density, and plasticity features, Proteins 79 (9) (2011) 2671–2683.
[47] Y. Xu, G.K. Kong, J.G. Menting, M.B. Margetts, C.A. Delaine, L.M. Jenkin, V. V. Kiselyov, P. De Meyts, B.E. Forbes, M.C. Lawrence, How ligand binds to the type 1 insulin-like growth factor receptor, Nat. Commun. 9 (1) (2018) 821.
[48] T.I. Croll, B.J. Smith, M.B. Margetts, J. Whittaker, M.A. Weiss, C.W. Ward, M. C. Lawrence, Higher-resolution structure of the human insulin receptor Ectodomain: multi-modal inclusion of the insert domain, Structure 24 (3) (2016) 469–476.
[49] F. Weis, J.G. Menting, M.B. Margetts, S.J. Chan, Y. Xu, N. Tennagels, P. Wohlfart, T. Langer, C.W. Muller, M.K. Dreyer, M.C. Lawrence, The signalling conformation of the insulin receptor ectodomain, Nat. Commun. 9 (1) (2018) 4420.
[50] T. Gutmann, I.B. Schafer, C. Poojari, B. Brankatschk, I. Vattulainen, M. Strauss, U. Coskun, Cryo-EM structure of the complete and ligand-saturated insulin receptor ectodomain, J. Cell Biol. 219 (1) (2020).
[51] Y. Xu, M.B. Margetts, H. Venugopal, J.G. Menting, N.S. Kirk, T.I. Croll, C. Delaine, B.E. Forbes, M.C. Lawrence, How insulin-like growth factor I binds to a hybrid insulin receptor type 1 insulin-like growth factor receptor, Structure 30 (8) (2022).
[52] B.G. Ziu Liu, Srayanta Mukherjee, Chengxin Zhang, Aysam Guerler, Jeffrey Brender, Zhiping Weng, Dong-Jun Yu, Yang Zhang, Full-length Protein Quaternary Structure Prediction by Multi-Chain Threading Fragment Reassembly, Submitted, 2022.
[53] S. Wu, Y. Zhang, MUSTER: improving protein sequence profile-profile alignments by using multiple sources of structure information, proteins: structure, Funct. Bioinform. 72 (2) (2008) 547–556.
[54] E. Krissinel, K. Henrick, Inference of macromolecular assemblies from crystalline state, J. Mol. Biol. 372 (3) (2007) 774–797.
[55] EMBL-EBI, Protein interfaces, surfaces and assemblies service PISA at the European Bioinformatics Institute (PDBePISA). http://www.ebi.ac.uk/pdbe/prot_int/pistart.html, 2021 (Accessed 13/04/2021 2021).
[56] E.S. Day, S.M. Cote, A. Whitty, Binding efficiency of protein–protein complexes, Biochemistry 51 (45) (2012) 9124–9136.
[57] J. Jumper, R. Evans, A. Pritzel, T. Green, M. Figurnov, O. Ronneberger, K. Tunyasuvunakool, R. Bates, A. Žídek, A. Potapenko, A. Bridgland, C. Meyer, S.A. A. Kohl, A.J. Ballard, A. Cowie, B. Romera-Paredes, S. Nikolov, R. Jain, J. Adler, T. Back, S. Petersen, D. Reiman, E. Clancy, M. Zielinski, M. Steinegger, M. Pacholska, T. Berghammer, S. Bodenstein, D. Silver, O. Vinyals, A.W. Senior, K. Kavukcuoglu, P. Kohli, D. Hassabis, Highly accurate protein structure prediction with AlphaFold, Nature 596 (7873) (2021) 583–589.
[58] A. Waterhouse, M. Bertoni, S. Bienert, G. Studer, G. Tauriello, R. Gumienny, F. T. Heer, T.A.P. de Beer, C. Rempfer, L. Bordoli, R. Lepore, T. Schwede, SWISS-MODEL: homology modelling of protein structures and complexes, Nucleic Acids Res. 46 (W1) (2018) W296–W303.
[59] Y. Haddad, V. Adam, Z. Heger, Ten quick tips for homology modeling of high-resolution protein 3D structures, PLoS Comput. Biol. 16 (4) (2020) e1007449.
[60] D.E. Scott, A.R. Bayly, C. Abell, J. Skidmore, Small molecules, big targets: drug discovery faces the protein–protein interaction challenge, Nat. Rev. Drug Discov. 15 (8) (2016) 533–550.
[61] J.C. Mitchell, KFC Server. https://mitchell-web.ornl.gov/KFC_Server/index.php (Accessed 04/03/2021).
[62] S.J. Darnell, L. Legault, J.C. Mitchell, KFC server: interactive forecasting of protein interaction hot spots, Nucleic Acids Res. 36 (Web Server) (2008) W265–W269.
[63] O. Keskin, A. Gursoy, B. Ma, R. Nussinov, Principles of protein−protein interactions: what are the preferred ways for proteins to interact? Chem. Rev. 108 (4) (2008) 1225–1244.
[64] P.D. Stenson, E.V. Ball, M. Mort, A.D. Phillips, J.A. Shiel, N.S. Thomas, S. Abeysinghe, M. Krawczak, D.N. Cooper, Human gene mutation database (HGMD): 2003 update, Hum. Mutat. 21 (6) (2003) 577–581.
[65] T. Kadowaki, C.L. Bevins, A. Cama, K. Ojamaa, B. Marcus-Samuels, H. Kadowaki, L. Beitz, C. McKeon, S.I. Taylor, Two mutant alleles of the insulin receptor gene in a patient with extreme insulin resistance, Science 240 (4853) (1988) 787–790.
[66] M. de Kerdanet, M. Caron-Debarle, S. Nivot, T. Gaillot, O. Lascols, B. Fremont, M. Bonaure, S. Gie, C. Massart, J. Capeau, Ten-year improvement of insulin resistance and growth with recombinant human insulin-like growth factor 1 in a patient with insulin receptor mutations resulting in leprechaunism, Diabetes Metab. 41 (4) (2015) 331–337.
[67] C. Blanquart, C. Gonzalez-Yanes, T. Issad, Monitoring the activation state of insulin/insulin-like growth factor-1 hybrid receptors using bioluminescence resonance energy transfer, Mol. Pharmacol. 70 (5) (2006) 1802–1811.
[68] V.V. Kiselyov, S. Versteyhe, L. Gauguin, P. De Meyts, Harmonic oscillator model of the insulin and IGF1 receptors' allosteric binding and activation, Mol. Syst. Biol. 5 (2009) 243.
[69] J.J. Wu, G. Guidotti, Proreceptor dimerization is required for insulin receptor post-translational processing, J. Biol. Chem. 279 (24) (2004) 25765–25773.
[70] Y.B. Xu, G.K.W. Kong, J.G. Menting, M.B. Margetts, C.A. Delaine, L.M. Jenkin, V. V. Kiselyov, P. De Meyts, B.E. Forbes, M.C. Lawrence, How ligand binds to the type 1 insulin-like growth factor receptor, Nat. Commun. 9 (2018).
[71] G. Scapin, V.P. Dandey, Z.N. Zhang, W. Prosise, A. Hruza, T. Kelly, T. Mayhood, C. Strickland, C.S. Potter, B. Carragher, Structure of the insulin receptor-insulin complex by single-particle cryo-EM analysis, Nature 556 (7699) (2018) 122.